



Persistent luminescence of inorganic nanophosphors prepared by wet-chemical synthesis



Everton Bonturim^{a,*}, Leonnam Gotardo Merízio^b, Roberto dos Reis^c,
Hermi Felinto Brito^b, Lucas Carvalho Veloso Rodrigues^b,
Maria Claudia França Cunha Felinto^a

^a Nuclear and Energy Research Institute, IPEN-CNEN/SP, University of São Paulo – USP, São Paulo, SP, Brazil

^b Department of Fundamental Chemistry, Institute of Chemistry, University of São Paulo – USP, São Paulo, SP, Brazil

^c National Center for Electron Microscopy, Molecular Foundry, LBNL, Berkeley, CA, USA

ARTICLE INFO

Article history:

Received 3 July 2017

Received in revised form

23 October 2017

Accepted 24 October 2017

Keywords:

Persistent luminescence

Wet-chemical synthesis

Size control

Luminescent nanoparticles

Microwave-assisted reduction process

ABSTRACT

The synthesis of efficient nanosized persistent luminescence materials remains a challenge for the community. Paradoxically, due to the dependence of the point lattice defects and the persistent luminescence efficiency, the control of the defect formation, favorable when the materials are prepared at high temperatures, normally leads to particle growth and sintering. In this work, efficient nanosized rare earth doped disilicates $\text{Sr}_2\text{MgSi}_2\text{O}_7:\text{Eu}^{2+},\text{Dy}^{3+}$ were synthesized via three different wet-chemical methods taking advantages of the microwave-assisted reduction process as a support step to produce high-quality polycrystalline materials. The crystallite size of the sample showed to be smaller when the decomposition temperature of the precursors is higher and close to the phase formation energy. The excitation VUV spectroscopy indicated that despite being nanocrystalline, the materials optical band gap has just a small difference compared one to another. The reduction of Eu^{3+} to Eu^{2+} was successfully obtained, since the f-d interconfigurational transitions of $\text{Eu}^{2+} 4f^65d^1 \rightarrow 4f^7$ emission were observed in the blue region of the spectra. The persistent luminescence efficiency measured through its lasting decay time was close to the commercial materials references and with the advantage of having size control during the synthesis method that can lead to the size dependent applications of photonic materials.

© 2017 Elsevier B.V. All rights reserved.

1. Introduction

Persistent luminescence is a class of luminescent phenomena comprehending the emission of electromagnetic radiation in a visible or NIR wavelength range for a prolonged period (from a couple seconds to many hours) after the stoppage of irradiation. Due to the imperfections that exist in any crystal structure, the charge carriers coming from the irradiation process play an important role in trapping–detrapping processes, increasing by this way the duration of the persistent luminescence [1–3].

This particular case of thermostimulated luminescence phenomenon has been observed over the past millennium and has been extensively studied since Vincenzo Cascariolo's discovery of the barite (BaSO_4), a sulfate mineral which exhibit persistent

luminescence after its reduction process to BaS (named Bologna stone) [4,5]. In this case, the emission came from the impurities of Cu^+ , which was both the activator and the defect generator for the energy storage [5]. Through the history of the phosphors, some compounds, spotted due their persistent luminescence efficiency, including the Eu^{2+} -doped aluminates MAl_2O_4 ($\text{M} = \text{Ca}, \text{Sr}, \text{Ba}$) [6–9], which have been investigated since its discovery in 1996, and the Eu-doped Rare Earth (RE)-codoped disilicates $\text{M}_2\text{MgSi}_2\text{O}_7$ [1,7,10–13], known for their very long persistent emission. Recently, a few compounds such as the gallates, stannates, oxysulfides, etc., have been developed to achieve a long-wavelength emission/excitation (VIS–NIR) persistence [14–16]. These compounds are widely applied as the materials for safety/emergency signs, road luminescent paints, displays and theranostic applications supported by *in-vivo* biomarkers [5,17–20].

The synthesis methods of inorganic compounds play an important role in determining fundamental characteristics of particles, such as particle morphology, porosity, crystallite size,

* Corresponding author.

E-mail address: ebonturim@usp.br (E. Bonturim).

homogeneity of composition, defects distribution, etc. Since the solid-state reactions (i.e. ceramic method) are the easiest way to prepare oxide materials, a huge amount of materials has been prepared by heating the mixture of powdered raw precursors. However, these methods require a long heat treatment at high temperatures to form the desired product. This method normally creates large particle agglomerates with irregular morphology and heterogeneity, bringing disadvantages to photonic materials, once the luminescent properties are strongly dependent on these parameters [1,18,19]. In the meanwhile, wet-chemical methods such as sol-gel [20–23], combustion [1,24–26], hydrothermal [27–29], co-precipitation [30–32], modified-Pechini [33–36] and so on, show great potential to prepare nanoparticles with reasonable control of parameters [18,37].

Particularly, the strontium magnesium disilicate $\text{Sr}_2\text{MgSi}_2\text{O}_7:\text{Eu}^{2+},\text{Dy}^{3+}$ has been widely studied due its chemical stability [38] and very long persistent luminescence showing the Eu^{2+} broad emission band centered around 460 nm (the blue region of the spectrum) [39,40]. The luminescence mechanism of Eu^{2+} doped $\text{Sr}_2\text{MgSi}_2\text{O}_7$ involves primarily the photoexcitation by UV–Vis radiation, promoting the electronic transitions $4f^7(^8\text{S}_{7/2}) \rightarrow 4f^65d^1$ where the $4f^65d^1$ excited state is partially overlapped with the conduction band (CB) of matrix. Thus, charge carriers, i.e. the excited electrons, can be delocalized to the conduction band and trapped by lattice defects into the host crystal. Finally, these electrons are thermally detrapped as a function of $k_B T$ recombining to the emitting ion [1,37,38].

The aim of this study is to understand the influence of different wet-chemical methods on the efficiency of disilicate $\text{Sr}_2\text{MgSi}_2\text{O}_7:\text{Eu}^{2+},\text{Dy}^{3+}$ nanoparticles. We have chosen the well-known modified-Pechini method, the complexation method using citric acid and oxalic acid with two different routes and the condensation method to prepare the material. Besides, we propose a microwave-assisted reduction process to speed up and enhance the conversion of Eu^{3+} to Eu^{2+} . In order to obtain the necessary data to explain crystallographic, morphologic, chemical and spectroscopic properties, these materials were investigated by thermogravimetric analysis (TG), X-ray powder diffraction (XPD), nanoparticle tracking analysis (NTA), instrumental neutron activation analysis (INAA) and VUV-UV-visible luminescence spectroscopy.

2. Experimental

2.1. Materials synthesis

Persistent luminescence nanoparticles of $\text{Sr}_2\text{MgSi}_2\text{O}_7:\text{Eu}^{2+},\text{Dy}^{3+}$ were prepared by three different wet-chemical routes: 1) modified-Pechini method; 2) complexation method and 3) condensation method, starting from the tetraethoxysilane ($\text{SiC}_8\text{H}_{20}\text{O}_4$ - TEOS), magnesium nitrate ($\text{Mg}(\text{NO}_3)_2 \cdot 6\text{H}_2\text{O}$), strontium nitrate ($\text{Sr}(\text{NO}_3)_2$) and rare earth nitrates ($\text{R}(\text{NO}_3)_3 \cdot 6\text{H}_2\text{O}$, $\text{R} = \text{Eu}^{3+}$ and Dy^{3+}). For these three methods, the ethanolic silica-based precursor solution was stirred along with the alkaline and rare earth nitrate aqueous solutions at 90 °C for 2 h, nitric acid and ammonium hydroxide were used to adjust the pH of the mixture to around 4. After a clear and translucent liquid was obtained, the solution was maintained in stirring at 70 °C for 15 h until a complete sol-gel reaction occurred. The Condensation method samples corresponds to this initial solution without any other reagent. For the Pechini method, samples were prepared by a mixing the proportion of 60:40 of citric acid ($\text{C}_6\text{H}_8\text{O}_7$ - 99.5%, Sigma-Aldrich) and ethylene glycol ($\text{C}_2\text{H}_6\text{O}_2$ - 99.8%, Sigma-Aldrich) into the initial solution described above. The metal ions and citric acid ratio varied as (1:1), (2:3) and (1:2). Finally, for the Complexation method, samples were prepared by a

mixture of either citric acid or oxalic acid ($\text{C}_2\text{H}_2\text{O}_4$ - 99%, Merck) with the initial solution using (1:2) of metal ions-complexation agent ratio. For all the methods, after the mixing, all solutions were stirred once again for another 2 h at 90 °C until the viscous gel became homogeneous. Then, the product was heat-treated at 300 °C for 2 h in a resistive furnace. The powder precursors were ground with a ceramic mortar and then calcined in alumina crucibles at different conditions, from 700 to 1200 °C for 1 and 5 h in air. Finally, the $\text{Sr}_2\text{MgSi}_2\text{O}_7:\text{Eu}^{3+},\text{Dy}^{3+}$ powders were reduced in a domestic microwave oven (Electrolux MEF41, 1000 W) using granular coal as the susceptor/reducing agent, at 700 W for 15 min. The scheme of the microwave-assisted reduction process used in this work is shown in Supplementary Fig. S1 and was previous well described by Pedroso et al.(2016) [19].

2.2. Characterization

Powder precursors of each synthesis method, before the calcination process, were studied via thermogravimetric analysis [41]. Thermal decomposition behavior, expressed by the mass losses as a function of the temperature, was carried out using a TGA-51H (Shimadzu) equipment. The raw precursors were heated using a platinum crucible, from 25 up to 1100 °C with a $10^\circ\text{C} \cdot \text{min}^{-1}$ rate, and a static air environment was used to simulate the furnace conditions during calcination process.

X-ray powder diffraction (XPD) [42] was carried out in a Rigaku Miniflex II diffractometer using a graphite monochromator with $K\alpha$ Cu radiation source ($\lambda = 1.5418 \text{ \AA}$). The polycrystalline sample patterns were scanned continuously in 2θ between 15 and 60° with a step of 0.02° and 1 s of integration time per point. The samples were prepared on a glass sample holder and measured at room temperature for all heat-treatment, calcination and reduction conditions, indicating the effect of the phase transition through the thermal processes of the material. The mean crystallite size of the samples after calcination and reduction processes were determined via mathematical correlation of the most intense (121) peak profile of the main Sr-åkermanite phase (well-adjusted by a Pseudo-Voigt function) into the Scherrer equation. The instrumental broadening corrections were made using the (222) peak of Y_2O_3 as the standard reference [43].

The nanoparticle tracking analysis (NTA) [44] was carried out with a NanoSight NS300 (Malvern) equipment using a 532 nm (green) laser source and a sCMOS sensor to detect the Brownian motion of the particles. The samples were dispersed in water at room temperature, sonicated during 1 min and collected using a syringe pump in a continuous flow into the sample holder of the optical system. The measurements were record with 25 FPS (frames per second), totaling 5 videos of 1 min each one for each sample.

Elemental distribution within the particles were analyzed by Energy Dispersive X-Ray (EDX) under Scanning Transmission Electron Microscopy (STEM) using a FEI -Titan microscope operating at 300 kV. High-Angle Annular Dark Field (HAADF) images were captured by a Fischione Model 3000 ADF detector. EDX spectra were collected by using a FEI SuperX quad windowless detector based on silicon drift technology with a solid angle of 0.7 steradian for about 15 min.

The concentration of rare earth elements present into the $\text{Sr}_2\text{MgSi}_2\text{O}_7:\text{Eu}^{2+},\text{Dy}^{3+}$ powders was obtained via Instrumental Neutron Activation Analysis (INAA) [45–47] carried out at the IEA-R1 Nuclear Research Reactor (located on the Research Reactor Center at IPEN-CNEN/SP). The samples were irradiated with a thermal neutron flux of $10^{13} \text{ cm}^{-2} \text{ s}^{-1}$ during 8 h, then a Canberra HPGe detector model GC2018 coupled to the Canberra DSA 1000 digital spectral analyzer was used to identify and quantify ^{153}Eu and ^{164}Dy radionuclides through the correspondent gamma ray decay.

The luminescence spectra (excitation and emission) and the persistent luminescence decay time were measured on a SPEX Fluorolog-2 spectrofluorometer using two 0.22 m SPEX1680 double-grating monochromators, a short-arc xenon lamp (450 W) as the irradiation source and a photomultiplier tube detector. Prior to the persistent luminescence decay time experiments, the samples were irradiated with 360 nm wavelength and then the emission was monitored at 460 nm. All the measurements were collected from powder pressed onto a sample holder placed at an angle of 22.5° (front face) at room temperature.

The synchrotron radiation spectroscopic studies were performed at the Brazilian Synchrotron Light Laboratory, Brazilian Center for Research in Energy and Materials, (LNLS–CNPEM), Campinas–SP, Brazil. The X-ray Absorption Near-Edge Structure (XANES) measurements of Eu element was measured at room temperature using the XAFS2 beamline. The data was collected in the fluorescence mode at room temperature on the Eu-L_{III} edge using the Si(111) double crystal monochromator with a 15-element Ge solid state detector (SSD). The energy resolution $\Delta E/E$ was 1.7×10^{-4} and the measured energy range was from 100 eV both before and after the edge. VUV–UV excitation spectra were recorded at room temperature from 4.2 to 8.2 eV, using a special quartz slide (thickness 200 μm), with an 8.2 eV cutoff (Act Ion – Tecnologia Científica). This filter was used to avoid the second order harmonics that come from the TGM beamline [48]. Signal was collected using an optical fiber connected to the R928 photomultiplier (Hamamatsu) and corrected using sodium salicylate as the standard reference [49]. A low-pass filter of 305 nm was used in front of the photomultiplier as an emission filter. The resolution in energy is $\Delta E/E = 700$, giving ca. 0.05 eV in the measured region.

3. Results and discussion

3.1. Thermal stability, phase and size analysis

The thermal stability of the disilicates synthesized in this work was evaluated according to their weight loss as a function of

temperature via thermogravimetric analyses. The thermogravimetric profile of all the samples has an initial stage of mass loss up to 100 °C corresponding to the desorption events of water molecules on the surface of the particles, mainly due humidity.

The samples prepared via modified-Pechini method (Fig. 1a–c) using different metal-citric acid ratios have a major loss of mass event around 480 °C related to the combustion/oxidation of the organic moiety, thus the loss of mass was proportional to the citric acid content in each ratio used. There is no other mass loss event present at higher temperatures, indicating that the thermal stability is achieved at low-temperature range. It means that an oxide structure is found above 550 °C for all Pechini prepared samples when the weight losses are not bigger than 4.5%. For the citric acid complexation method (Fig. 1d) there are two weight loss stages at 387 and 476 °C, corresponding to the decarboxylation processes of metal citrates and the decomposition of the carbonates by the formation of the oxide products [50]. Using oxalic acid as complexation agent (Fig. 1e), the first thermal decomposition of the possible oxalates is indicated by a multi-step stage of weight loss between 400 and 600 °C, followed by the formation of carbonates [51]. Then the oxide formation is reached at around 1050 °C. In the case of condensation method (Fig. 1f), a not well-defined intermediate stage related to the volatilization of the compounds from the non-stoichiometry condensation reaction of the TEOS can be observed up to 700 °C, when a major step of weight loss starts determined by the nitrates decomposition. Further details on the thermal events can be checked on the Supplementary Fig. S2. All the detailed assessment of the weight loss events for all the samples are summarized in Table 1.

Considering the phase formation kinetics of the disilicate, despite the high energy of phase transition, when the decomposition of the organic moiety takes place at lower temperatures, the materials prepared through Pechini and Citric acid methods, after being heated at 1000 °C, present majority Sr-åkermanite phase (shown in Fig. 2a–b). In the case of the oxalic acid and condensation methods, following the behavior observed in the TG data (Fig. 1e and f, respectively), even post-calcined at 1000 °C,

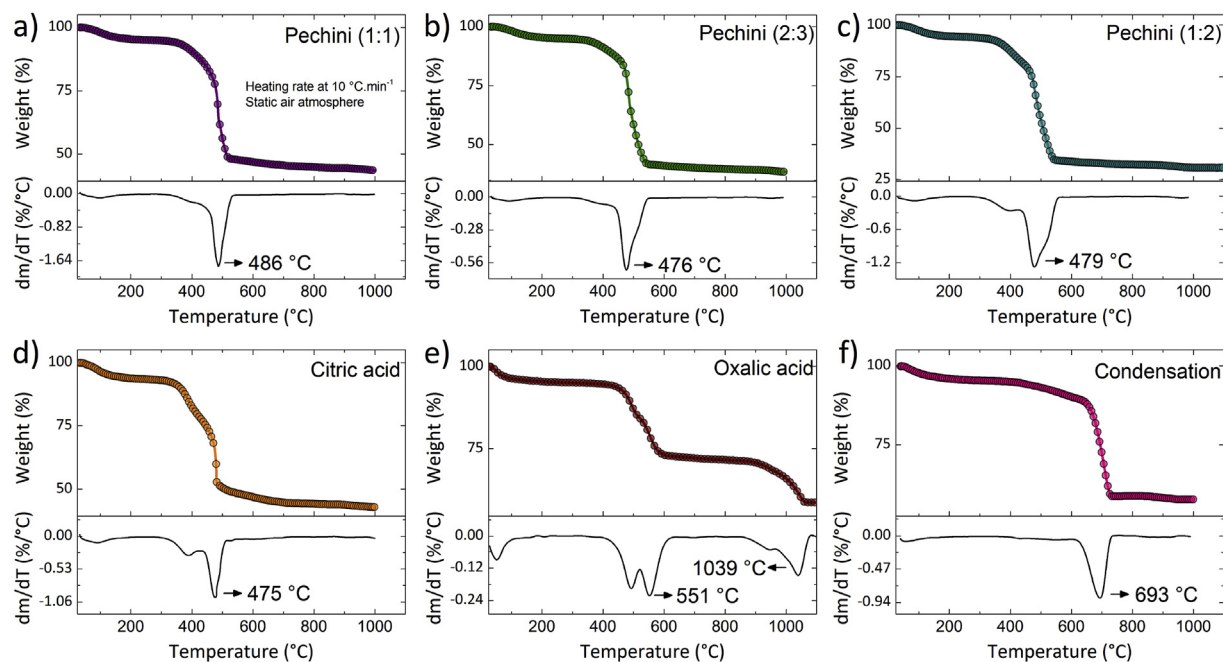


Fig. 1. Thermal decomposition behavior of as-synthesized powder of $\text{Sr}_2\text{MgSi}_2\text{O}_7:\text{Eu}^{3+},\text{Dy}^{3+}$ prepared by Pechini methods (a–c), complexation method using citric acid (d) and oxalic acid (e), condensation method of TEOS precursor (f) and their respective first derivative curves indicating the inflection points.

Table 1
Weight loss events and their onset temperatures (T_{onset}) of each TG step analyzed.

Synthesis method	Step range analyzed ^d			Weight loss (%)	Main released compounds
	T_i (°C)	T_f (°C)	ΔT_{onset} (°C)		
Pechini (1:1)	25	149	124	4.39	H ₂ O _(v) ^a
	361	477	116	12.12	H ₂ O _(v) and CO _(g) ^a
	477	516	39	34.16	CO _(g) and CO _{2(g)} ^a
	516	915	399	3.73	CO _{2(g)} ^a
	915	1000	85	0.76	
Pechini (2:3)	25	164	139	4.5	H ₂ O _(v) ^a
	359	472	113	9.6	H ₂ O _(v) and CO _(g) ^a
	472	544	72	43.46	CO _(g) and CO _{2(g)} ^a
	544	925	381	2.37	CO _{2(g)} ^a
	925	1000	75	0.87	
Pechini (1:2)	25	144	119	5.03	H ₂ O _(v) ^a
	346	468	122	15.75	H ₂ O _(v) and CO _(g) ^a
	468	542	74	43.61	CO _(g) and CO _{2(g)} ^a
	542	719	177	1.72	CO _{2(g)} ^a
	719	913	194	0.68	
Citric acid	25	192	167	6.24	H ₂ O _(v) ^{b,c,d}
	330	476	146	21.55	H ₂ O _(v) and CO _(g) ^{b,c,d}
	476	481	5	18.65	CO _(g) and CO _{2(g)} ^{b,c,d}
	481	683	202	8.07	CO _{2(g)} ^{b,c,d}
	683	895	212	0.72	
Oxalic acid	895	1000	105	1.08	
	25	97	72	4.3	H ₂ O _(v) ^{e,f,g}
	452	509	57	9.4	CO _(g) and CO _{2(g)} ^{e,f,g}
	509	535	26	2.28	CO _(g) and CO _{2(g)} ^{e,f,g}
	535	578	43	9.48	CO _(g) and CO _{2(g)} ^{e,f,g}
Condensation	578	969	391	2.74	CO _{2(g)} ^{e,f,g}
	969	1061	92	12.1	
	25	209	184	4.23	H ₂ O _(v) ^{h,i}
	416	668	252	6.81	H ₂ O _(v) and CO _(g) ^{h,i}
	668	843	175	29.27	NO _{x(g)} ^{h,i}
	843	950	107	1.03	CO _{2(g)} ^{h,i}

References on thermal decomposition compounds released:

^a Ref. [52].

^b Ref. [53].

^c Ref. [50].

^d Ref. [54].

^e Ref. [51].

^f Ref. [55].

^g Ref. [56].

^h Ref. [57].

ⁱ Ref. [58].

^j Parameters of TG analysis were obtained by the extrapolated onset temperature (T_{onset}) shown in details on Support information (Fig. S1).

crystallographic phase is not the pure disilicate one as shown in Supplementary Figs. S3 (e and f). This also reflects on the phase purity after 1200 °C followed by microwave dielectric heating (Fig. 3) where the products of the oxalic acid and condensation methods exhibit some impurity phase peaks mainly at 22.8, 27.4, 29.8, 31.1 and 32° (2 θ) and related to (Sr/Mg)SiO₄ and cristobalite phases formed in high temperatures, according the phase diagram of alkaline silicate glass materials. Besides that, two peaks located around 32.8 and 44° might be related due the presence of a high-temperature stable carbonate phase that is also verified in the FTIR spectra (Supplementary Fig. S4), exhibiting a characteristic band at ca. 1450 cm⁻¹ that can be assigned to the asymmetric stretching vibrations ν_3 of carbonate ions [59,60].

One great advantage of the wet-chemical methods to prepare inorganic materials is the possibility to control some synthesis parameters that allow you to engineer desirable characteristics in your material such as particle size and different morphologies. Thus, the particle size distribution determined by nanoparticle tracking analysis technique (Supplementary Fig. S5) indicates that the powder obtained via all the methods in this work are comprehended between 10 and 400 nm, taking into account the presence of agglomerates and aggregates for those large sizes due the

nature of the charge distribution on the surface and around the particles (described by the zeta potential).

Owing to the small size of the particles, we decided to compare the crystallite size and its particle sizes determined by NTA (Fig. 4). The estimation of the crystallite size was made using the mathematical approach of the Scherrer equation, considering the instrumental broadening as indicated in Experimental section.

It is possible to identify that the condensation method particles have a broader size distribution while the Pechini method yielded a sharper distribution in terms of the range between D10 and D90 fractions. Further investigation may lead a maneuvering to a better control of the agglomerate stabilization that creates larger particle sizing to D90 fraction of the size distribution. In the meanwhile, is expected for the Pechini method the narrow distribution since all the organic moiety leaves the precursor at lower temperature and the Sr-åkermanite phase starts to be formed before when compared with the Oxalic acid or the Condensation method. With the main phase being formed at lower temperatures, the thermodynamics plays a key role allowing the crystal growth mechanism. In the case of the condensation method, the Sr₂MgSi₂O₇ crystals are formed only at higher temperatures and there is not enough time for the particle growth, leading to a broad size distribution. However, this

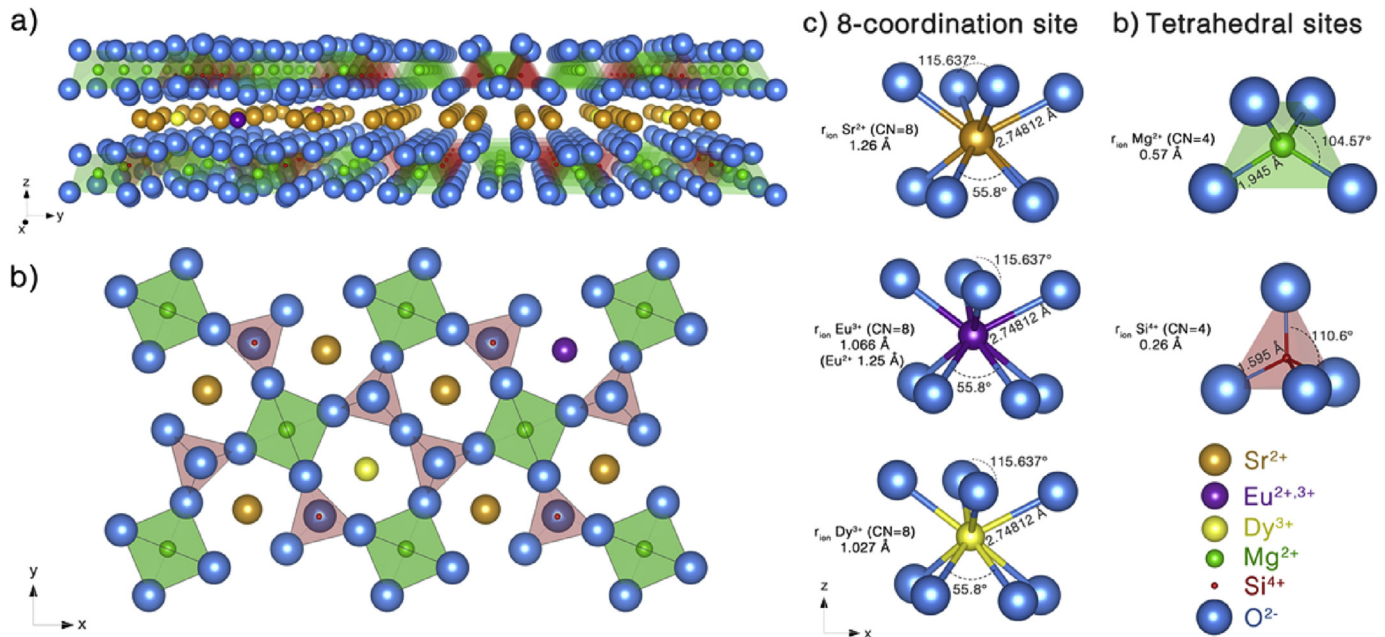


Fig. 2. Overall crystal structure of $\text{Sr}_2\text{MgSi}_2\text{O}_7:\text{Eu}^{3+}, \text{Dy}^{3+}$ phosphor in their perpendicular view from the (100) plane (a), a "top" view from the (001) plane showing the rare earth coordination positions and a detailed view of individual atoms and their bond lengths and angles in an 8-coordination site occupied by Sr^{2+} , $\text{Eu}^{2+,3+}$ and Dy^{3+} ions (c) and the tetrahedral sites occupied by the Si^{4+} and Mg^{2+} ions (d) into the Sr-åkermanite structure.

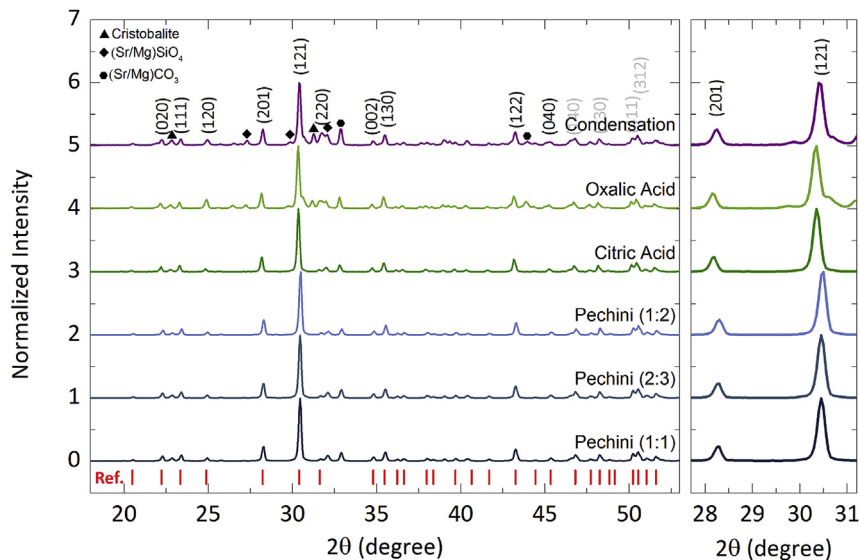


Fig. 3. X-ray powder diffraction data of $\text{Sr}_2\text{MgSi}_2\text{O}_7:\text{Eu}^{3+}, \text{Dy}^{3+}$ phosphors prepared by Pechini, complexation and condensation methods after a thermal treatment at 300 °C for 2 h, post-calcined at 1200 °C for 5 h in static air atmosphere and microwave-assisted reduction process. The (121) peaks used to determine crystallite sizes are detailed in the window on the right.

method yielded the smallest particles as indicated by the D50 fraction of the size distribution.

With respect to the size of the periodicity of the lattice, it is interesting to observe the correlation between the size of crystallite determined by the Scherrer method and the mean size distribution of the particles expressed through the D50 fraction of the NTA data for each sample (Fig. 4 – purple line/dots). In this case, there is a tendency in producing small particles and consequently small crystallites during its nucleation process. The samples obtained by the Condensation method compared with those obtained via Pechini method showed the smallest crystallite size.

Fig. 5 shows the HAADF images alongside its elemental mapping of the RE elements (Eu and Dy) for the Pechini (Fig. 5, top) and Condensation (Fig. 5, bottom) methods. The elemental maps show spatial distribution of the elements and depicts RE dopants more likely to be found at the edge of the particles. This indicates possible segregation of rare earths to the grain boundaries during the Pechini synthesis. Observation of the grain boundaries at high-resolution requires dose-efficient electron microscopy techniques due to the electron beam sensitive nature of the sample. It is important to notice here that the elemental maps show a homogeneous distribution of the chemical species other than the

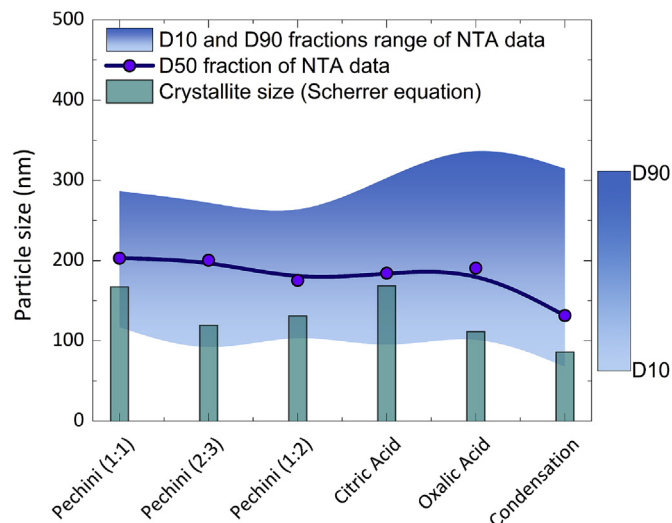


Fig. 4. Particle size distribution of $\text{Sr}_2\text{MgSi}_2\text{O}_7:\text{Eu}^{3+},\text{Dy}^{3+}$ phosphors obtained by NTA and expressed through its D10, D50 and D90 fractions (a) and the samples crystallite sizes for each kind of synthesis methods determined via Scherrer equation.

dopants (Supplementary Fig. S6).

3.2. Luminescence properties and persistent luminescence behavior

In solid state spectroscopy, two factors are crucial for the luminescent behavior of doped materials. The first aspect to consider is if all the dopants used in the synthesis are introduced within the final product. The second one is to determine the valence states of the dopant ions after the synthesis process ends. Only taking care of these two points, we can start to understand the atomic/electronic levels of the macroscopic events. Considering the need to know the efficiency of the low levels of doping used during the synthesis, the Instrumental Neutron Activation Analysis (INAA) (Supplementary Fig. S7) was used to measure the dopant

concentration in the sample after the calcination process at 1200 °C. The results obtained correspond to the nominal stoichiometry of both Eu and Dy dopant concentrations prior to the synthesis. In the case of the oxidation state of the dopants, only Dy^{3+} is stable, whereas, according to XANES data (Fig. 6c), both Eu^{2+} and Eu^{3+} states are possible to be found at substitutional positions of the Sr 8-coordinated sites (Fig. 2c) in the crystal structure even after the microwave-assisted reduction process. The tetrahedral sites (Fig. 2d) occupied by Mg^{2+} and Si^{4+} are too small to accommodate such a big ionic radius of RE elements, following the Goldschmidt tolerance factor (t) and Vegard's law to stabilize itself as a substitutional dopant with 8-fold coordination.

Independently on the concentration ratio of Eu^{3+} related to the Eu^{2+} , when both valences are present in a host lattice, the Eu^{2+} blue emission is dominant as shown in Fig. 6a–b due to two main reasons: i) the $\text{Eu}^{2+} 4f^65d^1 \rightarrow 4f^7$ interconfigurational transition is parity allowed, thus exhibiting higher intensity than the $4f^6 \rightarrow 4f^6$ intraconfigurational parity forbidden transitions of Eu^{3+} and ii) the allowed Eu^{2+} transitions have much faster lifetime (μs) compared to the Laporte forbidden Eu^{3+} ones (ms), thus suppressing the characteristic red emission of Eu^{3+} , as observed in some aluminates too [40].

The emission spectra of the materials prepared by different methods, calcined at 700, 1000 and 1200 °C, and microwave-assisting reduced have a broad profile (Fig. 7, right) with mainly the $\text{Eu}^{2+} 4f^65d^1 \rightarrow 4f^7$ emission present with maximum at 460 nm. It means that after the microwave dielectric heating, independent on the first furnace heating temperature, Eu^{3+} is reduced to Eu^{2+} (at least partially) (Fig. 6c). The similarity on the emission spectra profiles for all the samples (Fig. 7, right) indicate that Eu^{2+} occupies the same symmetry site surrounded by the crystal field of the C_5 point group of the Sr^{2+} site in the $\text{Sr}_2\text{MgSi}_2\text{O}_7$ host lattice.

The excitation spectra of all samples (Fig. 7, left) exhibit a broad absorption band with maximum around 360 nm, attributed to the $\text{Eu}^{2+} 4f^7 \rightarrow 4f^65d^1$ transition. This band is very broad due to mainly two reasons: i) the splitting of $5d^1$ state of Eu^{2+} which occupies a very low symmetry site, allowing the presence of up to 5 spectroscopic terms and ii) the very efficient process of persistent

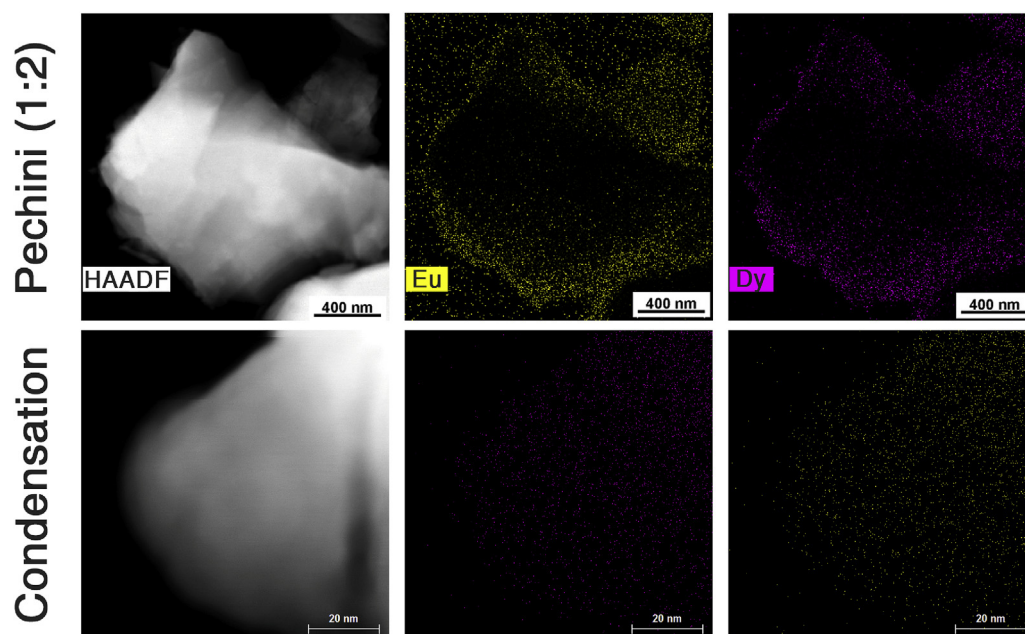


Fig. 5. 2D-elemental mapping of $\text{Sr}_2\text{MgSi}_2\text{O}_7:\text{Eu}^{2+},\text{Dy}^{3+}$ particles (Eu-L α and Dy-L α monitoring distribution are shown) synthesized by Pechini (top) and Condensation (bottom) methods.

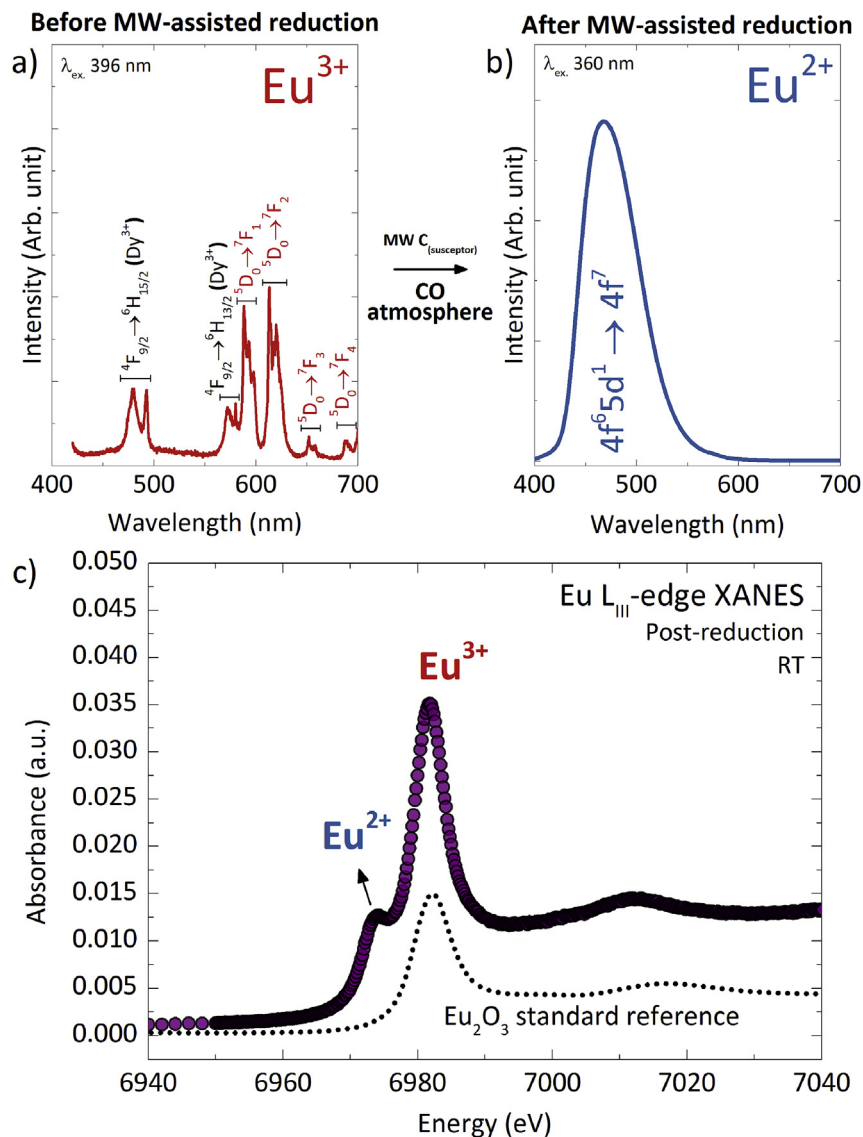


Fig. 6. Luminescence spectra of $\text{Sr}_{1.98}\text{MgSi}_2\text{O}_7:0.01\text{Eu}^{2+},0.01\text{Dy}^{3+}$ nanophosphor recorded at room temperature of the sample prepared via Pechini (1:2) method, calcined at $1200^\circ\text{C}/5\text{ h}$ before (a) and after (b) microwave-assisted reduction process, the XANES spectrum was recorded at Eu L_{III}-edge of the sample after reduction process (c) indicating the presence of Eu^{2+} species.

luminescence in this host lattice that broadens the excitation spectra [20].

The emission spectra of the 700°C calcined samples show a secondary band as a shoulder in the region around 600 nm for the oxalic acid and condensation methods (Fig. 7a). Since at 700°C the decomposition of these precursors is not complete the microwave heating not only reduces the europium ions but also decomposes the organic moiety at a reducing atmosphere, which might influence the formation of a secondary phase such as $\text{Sr}_2\text{SiO}_4:\text{Eu}^{2+}$. This band is less pronounced at the 1000°C heated oxalic acid sample, almost absent for the 1000°C condensation method (Fig. 7b) and almost completely absent for 1200°C oxalic acid and condensation samples (Fig. 7c), indicating that the smaller the quantity of organic and intermediate phases, the higher and purer will be the emission spectra due to the Eu^{2+} interconfigurational transition in $\text{Sr}_2\text{MgSi}_2\text{O}_7$ host.

Finally, it is possible to observe that the emission intensity difference of the samples prepared with different methods decrease with increasing heating temperature, especially for the methods

where the decomposition takes place at higher temperatures. This might be related to the crystallite size of the samples, since as discussed above, the particle size is smaller when the microwave heated samples do not have the final crystal structure, which is the case of the oxalic acid and condensation methods. One can observe that at 700°C (Fig. 7a), these two methods yields the most intense emission, but when the samples were heated at 1200°C and reduced via microwave-assisted method (Fig. 7c), the emission intensity difference became too small to quantitatively compare with one another.

The Synchrotron Radiation VUV excitation spectra (Fig. 8) measured at the TGM beamline of the Brazilian Synchrotron National Laboratory shows a subtle increase of the band gap energy of the calcined (at 1200°C) and reduced samples. The optical band gap energy of the materials in this work was determined using the maxima of the first derivative curves, the mathematical adjustments are shown in Supplementary Fig. S8. The maxima band gap energies measured were about 7.10(5) eV to the oxalic and condensation methods, similar to the values found in the literature

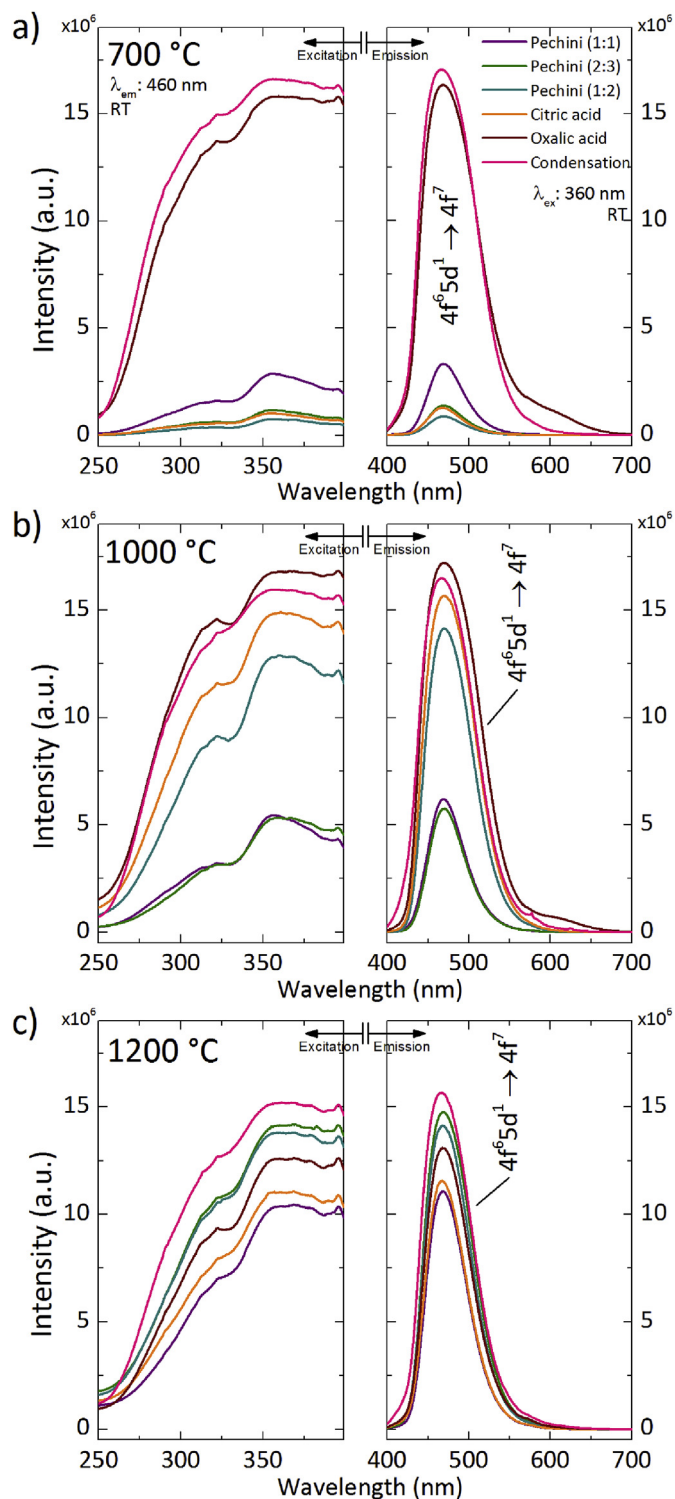


Fig. 7. Luminescence spectra (PL excitation – left, λ_{em} 460 nm; PL emission – right, λ_{ex} 360 nm) of $Sr_{1.98}MgSi_2O_7:0.01Eu^{2+},0.01Dy^{3+}$ nanophosphors recorded at room temperature of the samples prepared via Pechini, complexation and condensation methods, calcined at 700 °C/1 h (a), 1000 °C/1 h (b) and 1200 °C/5 h (c) and reduced by microwave-assisted process.

[20]. The lower band gap energies were determined for the Pechini and citric acid methods. The similarity between the band gap of all samples indicate that they have particles with sizes larger than tenths of nanometer, showing just a weak quantum effect in the

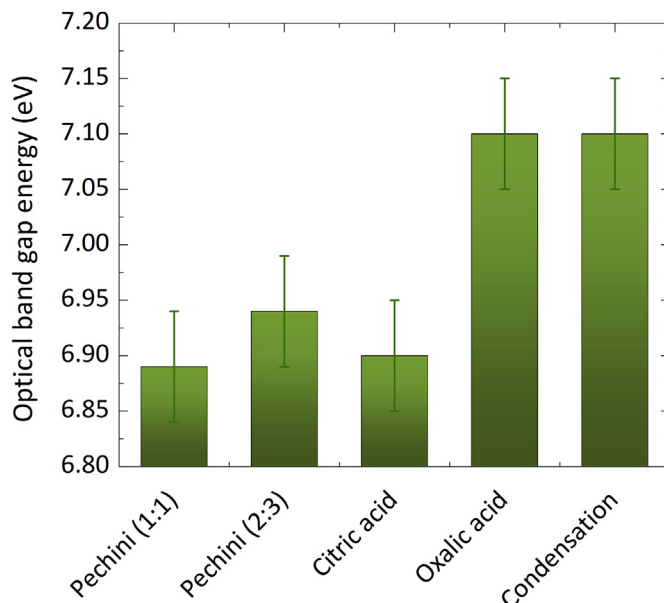


Fig. 8. Band gap energy of $Sr_{1.98}MgSi_2O_7:0.01Eu^{2+},0.01Dy^{3+}$ nanophosphors prepared by different wet-chemical routes defined by the mathematical adjustments of synchrotron radiation UV-VUV excitation spectra using the first derivative method.

band gap values due to their physical sizes, since it is still possible to observe an increase of the band gap energies with the decrease of the particle size. The band gap transition in this system corresponds to the transition between the filled O(2p) states from the valence band (VB) to the Sr(5s) empty states from the conduction band (CB).

The persistent luminescence decay curves (Fig. 9a–c) show that all the samples present considerable persistent luminescence time, visible even after 2 h after ceasing the irradiation source (Fig. 9d). The same behavior observed for the emission intensity difference (Fig. 7) where higher intensities for oxalic acid and condensation method for the samples calcined at the lowest temperature (700 °C), and similar to one another for those calcined at 1200 °C were observed in terms of the persistent luminescence decay times. At 1000 °C heating (Fig. 9a), the sample prepared via oxalic acid method exhibits persistent luminescence intensity one order of magnitude higher than the Pechini method samples, which is the least efficient material for this heat-treatment condition. However, when the 1200 °C samples are compared (Fig. 9b), the difference in the persistent luminescence efficiency is smaller, indicating that once the decomposition and phase formation temperatures are reached, the samples prepared via different methods start to behave similarly. Besides, one might observe that the samples prepared at 1200 °C are more efficient than the 1000 °C (Fig. 9c). This optical feature occurs due to the higher heating temperature, that favors the lattice defect formation, increasing its concentration. The defect formation is favored at high temperatures because it is as an endothermic process (creating vacancy sites require breaking ionic or, in some cases, covalent bonds in the solid state) with positive entropy variation (gaseous compounds are formed) [61]. Since the point defect concentration (e.g. oxygen vacancies) is related to the energy storage efficiency in persistent luminescence materials, the samples calcined at high temperatures (i.e. 1200 °C) will trap more electrons into their lattice defects, promoting a longer persistent luminescence emission process.

The materials prepared with the wet-chemical methods heated at 1200 °C followed by the microwave dielectric treatment showed a longer duration of the persistent luminescence than the solid-state prepared material (Fig. 9c) and similar behavior than the

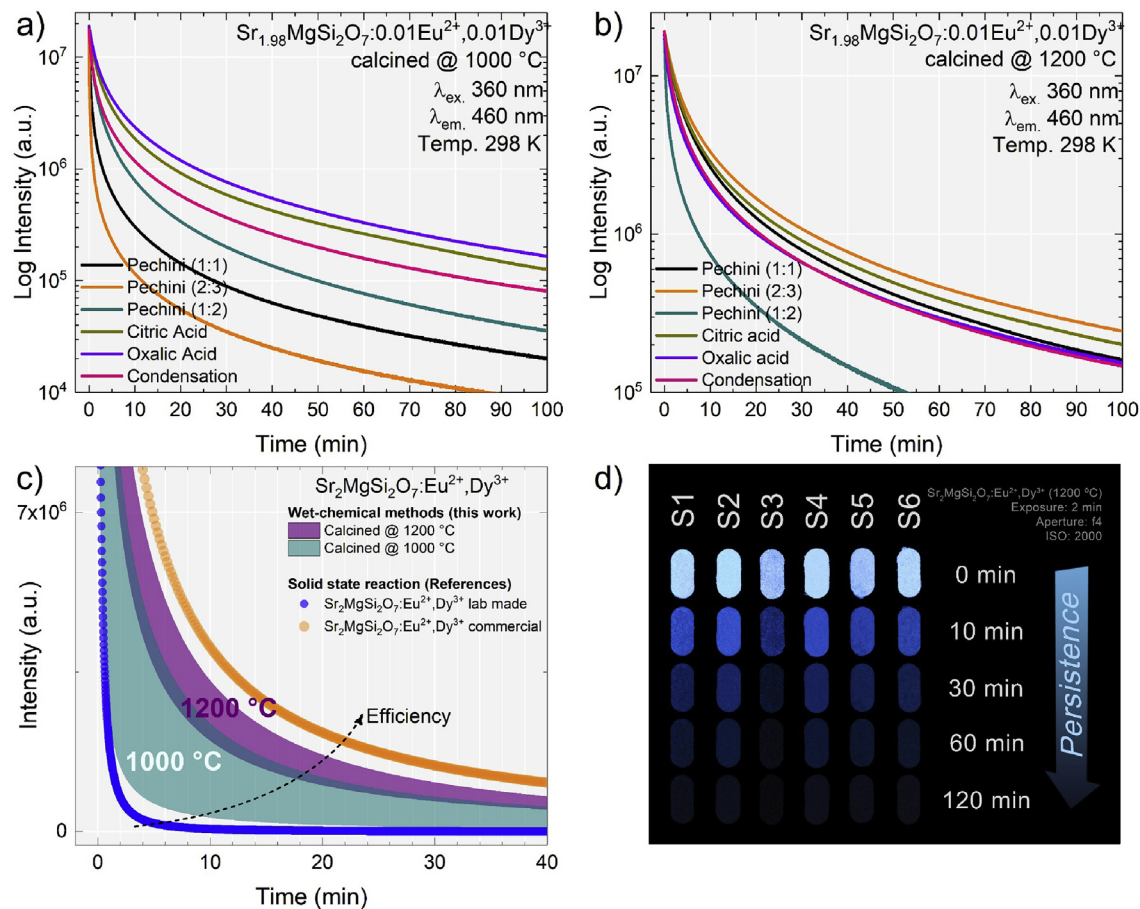


Fig. 9. Decay of persistent luminescence. (a) of Sr_{1.98}MgSi₂O₇:0.01Eu²⁺, 0.01Dy³⁺ nanophosphors prepared by different wet-chemical routes calcined at 1000 (a) and 1200 °C (b), the comparison between the upper and lower limits of group of samples for each calcination setup and with two references prepared by solid-state reaction (Sr₂MgSi₂O₇:Eu²⁺, Dy³⁺ lab made and commercial ones expressed by the blue and orange dots, respectively) (c) and the pictures of the samples (S1 – Pechini 1:1; S2 – Pechini 2:3; S3 – Pechini 1:2; S4 – Citric acid; S5 – Oxalic acid; S6 – Condensation method sample) in the dark as a function of the persistent decay time (d) registered with a professional camera in a manual setup to exposure of 2 min, aperture of f4 and ISO 2000. (For interpretation of the references to colour in this figure legend, the reader is referred to the web version of this article.)

commercial SrAl₂O₄:Eu²⁺, Dy³⁺ and Sr₂MgSi₂O₇:Eu²⁺, Dy³⁺ phosphors. In addition, these preparation methods present the advantage to have a higher particle size control, good stoichiometry and the lowest cost due to the reduction of the time and reagents (without H_{2(g)} consumption) to obtain the desired composition via microwave-assisted reduction process.

4. Conclusions

In summary, the wet-chemical routes experimented in this work proved to be an excellent pathway to obtain size controllable efficient persistent luminescence nanomaterials, which is desirable to the application process of the photonic materials such as the bioimaging technologies. The size control of the particles can be tuned by changing the parameters of synthesis or even the condensation precursors, following the empirical observation that demonstrated the higher the decomposition temperature of the precursor (close to the phase formation energy), smaller the final particle after the proper heat-treatments. This temperature is necessary to create more point defects that help the energy storage mechanisms of persistent luminescence phenomenon. The Sr₂MgSi₂O₇:Eu²⁺, Dy³⁺ wet-chemical prepared nanophosphors showed efficiency close to two very well-known solid-state commercial materials, with the advantage of having nanosized particles, which are more effective for several applications that depend

on dispersion, interaction or biocompatibility, such as luminescent paints, security signs and biotracers.

Acknowledgements

The authors acknowledge financial support from the Conselho Nacional de Desenvolvimento Científico e Tecnológico – CNPq (Process N.142266/2013-2) and Coordenação de Aperfeiçoamento de Pessoal de Nível Superior – CAPES (Process N.9511/2014-08). Work at the Molecular Foundry was supported by the Office of Science, Office of Basic Energy Sciences, of the U.S. Department of Energy under contract No. DE-AC02-05CH11231. The authors also thank Mr Olandir V. Correa who helped with the thermal analysis in Corrosion Lab on CCTM, Dr Edson G. Moreira who has executed the INAA measurements on the Research Reactor Center at IPEN-CNEN/SP, MSc Giordano T. Paganoto from the Molecular Spectroscopy Laboratory (LEM)/IQ-USP for the FTIR measurements and Dr Adriana F. Paes Leme and Dr Sami Yokoo for the support with the NTA analyses at (LNBio-CNPEM) (FAPESP#2010/19278-0). Finally, the authors also would like to thank Dr Veronica C. Teixeira, Dr Douglas Galante and Mr Leonardo M. Kofukuda (TGM beamline) and Dr Anna Levinsky and MSc Júnior Maurício (XAFS2 beamline) from the Brazilian Synchrotron Light Laboratory, Brazilian Center for Research in Energy and Materials, (LNLS-CNPEM), Campinas-SP, Brazil, for the measurements in the VUV-UV spectroscopy

(proposal TGM #20170461) and X-ray absorption spectroscopy (proposal XAFS1#17169) beamlines.

Appendix A. Supplementary data

Supplementary data related to this article can be found at <https://doi.org/10.1016/j.jallcom.2017.10.219>.

References

- [1] K. Van den Eeckhout, P.F. Smet, D. Poelman, Persistent luminescence in Eu^{2+} doped compounds: a review, *Materials (Basel)* 3 (2010) 2536–2566, <https://doi.org/10.3390/ma3042536>.
- [2] J. Hölsä, Persistent luminescence beats the afterglow: 400 Years of persistent luminescence, *Electrochem. Soc. Interface* 4 (2009) 42–45, http://www.electrochem.org/dl/interface/wtr/wtr09/wtr09_p042-045.pdf.
- [3] T. Aitasalo, P. Dereň, J. Hölsä, H. Jungner, J.-C. Krupa, M. Lastusaari, J. Legendziewicz, J. Niittykoski, W. Stręk, Persistent luminescence phenomena in materials doped with rare earth ions, *J. Solid State Chem.* 171 (2003) 114–122, [https://doi.org/10.1016/S0022-4596\(02\)00194-9](https://doi.org/10.1016/S0022-4596(02)00194-9).
- [4] P.F. Smet, I. Moreels, Z. Hens, D. Poelman, Luminescence in sulfides: a rich history and a bright future, *Materials (Basel)* 3 (2010) 2834–2883, <https://doi.org/10.3390/ma3042834>.
- [5] M. Lastusaari, T. Laamanen, M. Malkamäki, K.O. Eskola, A. Kotlov, S. Carlson, E. Welter, H.F. Brito, M. Bettinelli, H. Jungner, J. Hölsä, The Bologna Stone: history's first persistent luminescent material, *Eur. J. Mineral.* 24 (2012) 885–890, <https://doi.org/10.1127/0935-1221/2012/0024-2224>.
- [6] T. Matsuzawa, A new long phosphorescent phosphor with high brightness, $\text{SrAlO}_4:\text{Eu}^{2+}, \text{Dy}^{3+}$, *J. Electrochem. Soc.* 143 (1996) 2670, <https://doi.org/10.1149/1.1837067>.
- [7] Y. Lin, Z. Tang, Z. Zhang, C. Wen Nan, Luminescence of Eu and Dy activated $\text{R}_3\text{MgSi}_2\text{O}_8$ -based (R=Ca, Sr, Ba) phosphors, *J. Alloys Compd.* 348 (2003) 76–79, [https://doi.org/10.1016/S0925-8388\(02\)00796-X](https://doi.org/10.1016/S0925-8388(02)00796-X).
- [8] Y. Lin, Z. Zhang, Z. Tang, J. Zhang, Z. Zheng, X. Lu, The characterization and mechanism of long afterglow in alkaline earth aluminates phosphors co-doped by Eu_2O_3 and Dy_2O_3 , *Mater. Chem. Phys.* 70 (2001) 156–159, [https://doi.org/10.1016/S0254-0584\(00\)00500-9](https://doi.org/10.1016/S0254-0584(00)00500-9).
- [9] R. Sakai, T. Katsumata, S. Komuro, T. Morikawa, Effect of composition on the phosphorescence from $\text{BaAl}_2\text{O}_4:\text{Eu}^{2+}, \text{Dy}^{3+}$ crystals, *J. Lumin.* 85 (1999) 149–154, [https://doi.org/10.1016/S0022-2313\(99\)00061-7](https://doi.org/10.1016/S0022-2313(99)00061-7).
- [10] A.A.S. Alvani, F. Moztarzadeh, A.A.A. Sarabi, A.A. Sabbagh Alvani, F. Moztarzadeh, A.A.A. Sarabi, Effects of dopant concentrations on phosphorescence properties of Eu/Dy -doped $\text{Sr}_3\text{MgSi}_2\text{O}_8$, *J. Lumin.* 114 (2005) 131–136, <https://doi.org/10.1016/j.jlumin.2004.12.012>.
- [11] Y. Lin, Z. Tang, Z. Zhang, X. Wang, J. Zhang, Preparation of a new long afterglow blue-emitting $\text{Sr}_2\text{MgSi}_2\text{O}_7$ -based photoluminescent phosphor, *J. Mater. Sci. Lett.* 20 (2001) 1505–1506, <https://doi.org/10.1023/A:1017930630889>.
- [12] L. Jiang, C. Chang, D. Mao, C. Feng, Luminescent properties of $\text{CaMgSi}_2\text{O}_6$ -based phosphors co-doped with different rare earth ions, *J. Alloys Compd.* 377 (2004) 211–215, <https://doi.org/10.1016/j.jallcom.2004.01.024>.
- [13] T. Aitasalo, D. Hreniak, J. Hölsä, T. Laamanen, M. Lastusaari, J. Niittykoski, F. Pellé, W. Stręk, W. Stręk, Persistent luminescence of $\text{Ba}_2\text{MgSi}_2\text{O}_7:\text{Eu}^{2+}$, *J. Lumin.* 122–123 (2007) 110–112, <https://doi.org/10.1016/j.jlumin.2006.01.112>.
- [14] J. Xu, Z. Ju, X. Gao, Y. An, X. Tang, W. Liu, $\text{Na}_2\text{CaSn}_2\text{Ge}_3\text{O}_{12}$: a novel host lattice for Sm^{3+} -doped long-persistent phosphorescence materials emitting reddish orange light, *Inorg. Chem.* 52 (2013) 13875–13881, <https://doi.org/10.1021/ic401262w>.
- [15] W. Yan, F. Liu, Y. Lu, X. Wang, M. Yin, Z. Pan, Near infrared long-persistent phosphorescence in $\text{La}_3\text{Ga}_5\text{GeO}_{14}:\text{Cr}^{3+}$ phosphor, *Opt. Express* 18 (2010) 103–104, <https://doi.org/10.1364/OME.4.000638>.
- [16] Z. Pan, Y.-Y. Lu, F. Liu, Sunlight-activated long-persistent luminescence in the near-infrared from Cr^{3+} -doped zinc gallogermanates, *Nat. Mater.* 11 (2011) 58–63, <https://doi.org/10.1038/nmat3173>.
- [17] J. Yan, L. Ning, Y. Huang, C. Liu, D. Hou, B. Zhang, Y. Huang, Y. Tao, H. Liang, Luminescence and electronic properties of $\text{Ba}_2\text{MgSi}_2\text{O}_7:\text{Eu}^{2+}$: a combined experimental and hybrid density functional theory study, *J. Mater. Chem. C* 2 (2014) 8328–8332, <https://doi.org/10.1039/C4TC01332H>.
- [18] Y. Li, M. Gecevicius, J. Qiu, Long persistent phosphors—from fundamentals to applications, *Chem. Soc. Rev.* 45 (2016) 2090–2136, <https://doi.org/10.1039/C5CS00582E>.
- [19] C.C.S. Pedroso, J.M. Carvalho, L.C.V. Rodrigues, J. Hölsä, H.F. Brito, Rapid and energy-saving microwave-assisted solid-state synthesis of Pr^{3+} , Eu^{3+} , or Tb^{3+} -doped Lu_2O_3 persistent luminescence materials, *ACS Appl. Mater. Interfaces* 8 (2016) 19593–19604, <https://doi.org/10.1021/acsami.6b04683>.
- [20] X. Qu, L. Cao, W. Liu, G. Su, P. Wang, I. Schultz, Sol–gel synthesis of long-lasting phosphors $\text{CdSiO}_3:\text{Mn}^{2+}, \text{RE}^{3+}$ (RE=Tb, Eu, Nd) and luminescence mechanism research, *Mater. Res. Bull.* 47 (2012) 1598–1603, <https://doi.org/10.1016/j.materresbull.2011.08.012>.
- [21] S.K. Gupta, M. Mohapatra, S. Kaity, V. Natarajan, S.V. Godbole, Structure and site selective luminescence of sol–gel derived $\text{Eu}:\text{Sr}_2\text{SiO}_4$, *J. Lumin.* 132 (2012) 1329–1338, <https://doi.org/10.1016/j.jlumin.2012.01.011>.
- [22] D. Hreniak, W. Stręk, P. Mazur, R. Pazik, M. Ząbkowska-Waciawek, Luminescence properties of $\text{Tb}^{3+}:\text{Y}_3\text{Al}_5\text{O}_{12}$ nanocrystallites prepared by the sol–gel method, *Opt. Mater. (Amst)* 26 (2004) 117–121, <https://doi.org/10.1016/j.optmat.2003.11.008>.
- [23] P. Gluchowski, W. Stręk, M. Lastusaari, J. Hölsä, Optically stimulated persistent luminescence of europium doped LaAlO_3 nanocrystals, *Phys. Chem. Chem. Phys.* 17 (n.d.) 17246–17252, <https://dx.doi.org/10.1039/C5CP00234F>.
- [24] B. Cheng, Z. Zhang, Z. Han, Y. Xiao, S. Lei, $\text{SrAl}_x\text{O}_y:\text{Eu}^{2+}, \text{Dy}^{3+}$ (x = 4) nanostructures: structure and morphology transformations and long-lasting phosphorescence properties, *CrystEngComm* 13 (2011) 3545, <https://doi.org/10.1039/c0ce00934b>.
- [25] Y.J. Li, M.W. Wang, L.D. Zhang, D. Gao, S.X. Liu, Soft chemical synthesis and luminescence properties of red long-lasting phosphors $\text{Y}_2\text{O}_3:\text{Sm}^{3+}$, *Int. J. Min. Metall. Mater.* 20 (2013) 972–977, <https://doi.org/10.1007/s12613-013-0823-3>.
- [26] N. Yu, F. Liu, X. Li, Z. Pan, Near infrared long-persistent phosphorescence in $\text{SrAl}_2\text{O}_4:\text{Eu}^{2+}, \text{Dy}^{3+}, \text{Er}^{3+}$ phosphors based on persistent energy transfer, *Appl. Phys. Lett.* 95 (2009) 3–6, <https://doi.org/10.1063/1.3272672>.
- [27] D. Liu, C. Cui, P. Huang, L. Wang, G. Jiang, Luminescent properties of red long-lasting phosphor $\text{Y}_2\text{O}_3:\text{Eu}^{3+}, \text{M}^{2+}$ (M=Mg, Ca, Sr, Ba), Ti^{4+} nanotubes via hydrothermal method, *J. Alloys Compd.* 583 (2014) 530–534, <https://doi.org/10.1016/j.jallcom.2013.08.196>.
- [28] Y.-F. Xu, D.-K. Ma, M.-L. Guan, X.-A. Chen, Q.-Q. Pan, S.-M. Huang, Controlled synthesis of single-crystal $\text{SrAl}_2\text{O}_4:\text{Eu}^{2+}, \text{Dy}^{3+}$ nanosheets with long-lasting phosphorescence, *J. Alloys Compd.* 502 (2010) 38–42, <https://doi.org/10.1016/j.jallcom.2010.04.186>.
- [29] M. Zheng, X. Chen, B. Lei, Y. Xiao, R. Liu, H. Zhang, H. Dong, Y. Liu, X. Liu, Synthesis and luminescence properties of flower-like $\text{Sr}_2\text{MgSi}_2\text{O}_7:\text{Eu}^{2+}, \text{Dy}^{3+}$ phosphor via hydrothermal-homogeneous coprecipitation route, *ECS Solid State Lett.* 2 (2013) R19–R22, <https://doi.org/10.1149/2.008306ssl>.
- [30] W. Pan, G. Ning, X.X. Zhang, J. Wang, Y. Lin, J. Ye, Enhanced luminescent properties of long-persistent $\text{Sr}_2\text{MgSi}_2\text{O}_7:\text{Eu}^{2+}, \text{Dy}^{3+}$ phosphor prepared by the co-precipitation method, *J. Lumin.* 128 (2008) 1975–1979, <https://doi.org/10.1016/j.jlumin.2008.06.009>.
- [31] B. Cheng, H. Liu, M. Fang, Y. Xiao, S. Lei, L. Zhang, Long-persistent phosphorescent $\text{SrAl}_2\text{O}_4:\text{Eu}^{2+}, \text{Dy}^{3+}$ nanotubes, *Chem. Commun.* (2009) 944–946, <https://doi.org/10.1039/B818057A>.
- [32] Y. Liu, S.X. Liu, M.W. Wang, W.J. Li, T. Zhang, X. Zhang, Synthesis and luminescence properties of $\text{Eu}^{3+}, \text{Sm}^{3+}$ doped ($\text{Y}_x\text{Gd}_{1-x}$) $\text{O}_3:\text{Si}^{4+}, \text{Mg}^{2+}$ long-lasting phosphor, *Int. J. Min. Metall. Mater.* 17 (2010) 347–352, <https://doi.org/10.1007/s12613-010-0317-5>.
- [33] S.A.M. Lima, F.A. Sigoli, M.R. Davolos, M. Jafelicci, Europium(III)-containing zinc oxide from Pechini method, *J. Alloys Compd.* 344 (2002) 280–284, [https://doi.org/10.1016/S0925-8388\(02\)00369-9](https://doi.org/10.1016/S0925-8388(02)00369-9).
- [34] H. Zhang, X. Fu, S. Niu, G. Sun, Q. Xin, Photoluminescence of $\text{YVO}_4:\text{Tm}$ phosphor prepared by a polymerizable complex method, *Solid State Commun.* 132 (2004) 527–531, <https://doi.org/10.1016/j.ssc.2004.09.008>.
- [35] H. Zhang, X. Fu, S. Niu, Q. Xin, Synthesis and photoluminescence properties of Eu^{3+} -doped AZrO_3 (A=Ca, Sr, Ba) perovskite, *J. Alloys Compd.* 459 (2008) 103–106, <https://doi.org/10.1016/j.jallcom.2007.04.259>.
- [36] H. Zhang, X. Fu, S. Niu, Q. Xin, Blue luminescence of nanocrystalline $\text{CaZrO}_3:\text{Tm}$ phosphors synthesized by a modified Pechini sol–gel method, *J. Lumin.* 128 (2008) 1348–1352, <https://doi.org/10.1016/j.jlumin.2008.01.007>.
- [37] T. Aitasalo, J. Hassinen, J. Holsa, T. Laamanen, M. Lastusaari, M. Malkamäki, J. Niittykoski, P. Novák, J. Hölsä, T. Laamanen, M. Lastusaari, M. Malkamäki, J. Niittykoski, P. Novák, Synchrotron radiation investigations of the $\text{Sr}_2\text{MgSi}_2\text{O}_7:\text{Eu}^{2+}, \text{R}^{3+}$ persistent luminescence materials, *J. Rare Earths* 27 (2009) 529–538, [https://doi.org/10.1016/S1002-0721\(08\)60283-5](https://doi.org/10.1016/S1002-0721(08)60283-5).
- [38] L. Wondraczek, S. Krolkowski, P. Nass, Europium partitioning, luminescence re-absorption and quantum efficiency in (Sr,Ca) alkermanite–feldspar biphasic glass ceramics, *J. Mater. Chem. C* 1 (2013) 4078, <https://doi.org/10.1039/c3tc30609g>.
- [39] L.C.V. Rodrigues, H.F. Brito, J. Hölsä, M. Lastusaari, Persistent luminescence behavior of materials doped with Eu^{2+} and Tb^{3+} , *Opt. Mater. Express* 2 (2012) 382, <https://doi.org/10.1364/OME.2.000382>.
- [40] E. Finley, A. Cobb, A. Duke, A. Paterson, J. Brgoch, Optimizing blue persistent luminescence in $(\text{Sr}_{1-x}\text{Ba}_x)_2\text{MgSi}_2\text{O}_7:\text{Eu}^{2+}, \text{Dy}^{3+}$ via solid solution for use in point-of-care diagnostics, *ACS Appl. Mater. Interfaces* 8 (2016) 26956–26963, <https://doi.org/10.1021/acsami.6b10303>.
- [41] S. Vyazovkin, Thermogravimetric analysis, in: *Charact. Mater.*, John Wiley & Sons, Inc., Hoboken, NJ, USA, 2012, <https://doi.org/10.1002/0471266965.com029.pub2>.
- [42] B.D. Cullity, *Elements of X-ray diffraction*, Addison-Wesley Publishing Company, Massachusetts, 1956.
- [43] L.G. Martinez, R.U. Ichikawa, K. Imakawa, X. Turrillas, Standard reference materials for powder diffraction developed at IPEN/CNEN – Brazil, in: *IX Reun. Anu. La Asoc. Argentina Cristalogr. Y I Reun. Latinoam. Cristalogr., Asociación Argentina de Cristalografía, Ciudad de Córdoba, 2013*, <https://doi.org/10.13140/RG.2.1.4293.2322>.
- [44] V. Filipe, A. Have, W. Jiskoot, Critical evaluation of nanoparticle tracking analysis (NTA) by NanoSight for the measurement of nanoparticle and protein aggregates, *Pharm. Res.* 27 (2010) 796–810, <https://doi.org/10.1007/s11095-010-0073-2>.
- [45] P. Bode, E.A. De Nadai Fernandes, R.R. Greenberg, Metrology for chemical measurements and the position of INAA, *J. Radioanal. Nucl. Chem.* 245 (2000)

- 109–114, <https://doi.org/10.1023/A:1006752509734>.
- [46] R.R. Greenberg, P. Bode, E.A. De Nadai Fernandes, Neutron activation analysis: a primary method of measurement, *Spectrochim. Acta Part B At. Spectrosc.* 66 (2011) 193–241, <https://doi.org/10.1016/j.sab.2010.12.011>.
- [47] V.P. Guinn, C.D. Wagner, Instrumental neutron activation analysis, *Anal. Chem.* 32 (1960) 317–323, <https://doi.org/10.1021/ac60159a005>.
- [48] R.L. Cavasso Filho, A.F. Lago, M.G.P. Homem, S. Pilling, A. Naves de Brito, Delivering high-purity vacuum ultraviolet photons at the Brazilian toroidal grating monochromator (TGM) beamline, *J. Electron Spectros. Relat. Phenom.* 156–158 (2007) 168–171, <https://doi.org/10.1016/j.elspec.2006.11.026>.
- [49] T. Aitasalo, J. Hölsä, M. Kirm, T. Laamanen, M. Lastusaari, J. Niittykoski, J. Raud, R. Valtonen, Persistent luminescence and synchrotron radiation study of the $\text{Ca}_2\text{MgSi}_2\text{O}_7:\text{Eu}^{2+},\text{R}^{3+}$ materials, *Radiat. Meas.* 42 (2007) 644–647, <https://doi.org/10.1016/j.radmeas.2007.01.058>.
- [50] S.A.A. Mansour, Thermal decomposition of calcium citrate tetrahydrate, *Thermochim. Acta* 233 (1994) 243–256, [https://doi.org/10.1016/0040-6031\(94\)85118-2](https://doi.org/10.1016/0040-6031(94)85118-2).
- [51] H.A. Papazian, P.J. Pizzolato, J.A. Patrick, Thermal decomposition of oxalates of ammonium and potassium, *J. Am. Ceram. Soc.* 54 (1971) 250–254, <https://doi.org/10.1111/j.1151-2916.1971.tb12282.x>.
- [52] H. He, R. Fu, H. Wang, X. Song, Z. Pan, X. Zhao, X. Zhang, Y. Cao, $\text{Li}_2\text{SrSiO}_4:\text{Eu}^{2+}$ phosphor prepared by the Pechini method and its application in white light emitting diode, *J. Mater. Res.* 23 (2008) 3288–3294, <https://doi.org/10.1557/JMR.2008.0394>.
- [53] M.M. Barbooti, D.A. Al-Sammerrai, Thermal decomposition of citric acid, *Thermochim. Acta* 98 (1986) 119–126, [https://doi.org/10.1016/0040-6031\(86\)87081-2](https://doi.org/10.1016/0040-6031(86)87081-2).
- [54] A. Srivastava, P. Singh, V.G. Gunjkar, A.P.B. Sinha, Study of the thermal decomposition of iron and barium citrates, *Thermochim. Acta* 86 (1985) 77–84, [https://doi.org/10.1016/0040-6031\(85\)87035-0](https://doi.org/10.1016/0040-6031(85)87035-0).
- [55] W.W. Wendlandt, Thermal decomposition of rare earth metal oxalates, *Anal. Chem.* 31 (1959) 408–410, <https://doi.org/10.1021/ac60147a024>.
- [56] D. Dollimore, The thermal decomposition of oxalates: a review, *Thermochim. Acta* 117 (1987) 331–363, [https://doi.org/10.1016/0040-6031\(87\)88127-3](https://doi.org/10.1016/0040-6031(87)88127-3).
- [57] L. He, B. Jia, L. Che, W. Li, W. Sun, Preparation and optical properties of afterglow $\text{Sr}_2\text{MgSi}_2\text{O}_7:\text{Eu}^{2+},\text{Dy}^{3+}$ electrospun nanofibers, *J. Lumin.* 172 (2016) 317–322, <https://doi.org/10.1016/j.jlumin.2015.12.012>.
- [58] C.J. Brinker, Hydrolysis and condensation of silicates: effects on structure, *J. Non. Cryst. Solids* 100 (1988) 31–50, [https://doi.org/10.1016/0022-3093\(88\)90005-1](https://doi.org/10.1016/0022-3093(88)90005-1).
- [59] B.E. Scheetz, W.B. White, Vibrational spectra of the alkaline earth double carbonates, *Am. Mineral.* 62 (1977) 36–50.
- [60] S. Gunasekaran, G. Anbalagan, S. Pandi, Raman and infrared spectra of carbonates of calcite structure, *J. Raman Spectrosc.* 37 (2006) 892–899, <https://doi.org/10.1002/jrs.1518>.
- [61] A. Paul, T. Laurila, V. Vuorinen, S.V. Divinski, *Thermodynamics, Diffusion and the Kirkendall Effect in Solids*, Springer International Publishing, Cham, 2014, <https://doi.org/10.1007/978-3-319-07461-0>.